UNIVERSITY OF TWENTE.

Faculty of Engineering Technology

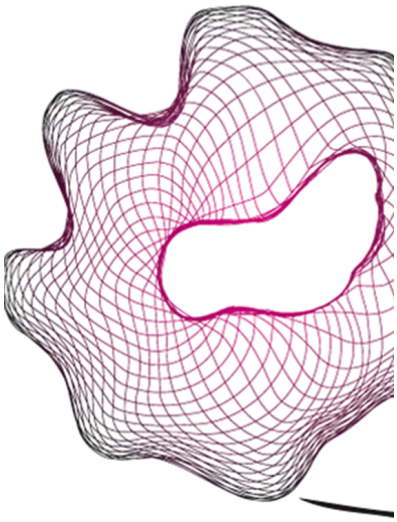

Development of a low-cost FSO ground station

"A manipulator to steer a mirror that makes the communication laser track the satellite."

June 26, 2020

Group 15:
Tom Edelijn (s2166461)
Bas Hemeltjen (s1976567)
Henk Jekel (s1802178)
Gijs Oude Vrielink (s1996185)
Lisse Reef (s2007606)
Jan Maarten Schaapman (s2143666)

University of Twente
P.O. Box 217
7500 AE Enschede
The Netherlands

Contents

1 Introduction

Free space optical communication is used to transmit optical data from ground to space. Communication can be realized by multiple different methods. In this case a laser is used. In order to use such a communication system, a ground station has to be designed allowing low-cost space operation. To successfully track satellites with a laser, a mirror has to be manipulated with a mechatronic system that is powered by a VCM actuator. In this report, a mechatronic system is designed which must satisfy a set of requirements. Later, this design is validated.

2 Concept

To be able to deliver a design, it should first be conceptualized, which is done in this section.

2.1 Requirements

The design has to meet prescribed requirements. The five most important requirements are listed below.

R.1 The design should be a one degree of freedom system.

R.2 The manipulator should rotate the mirror at a speed of 19.5 mrad/s and the satellite should be tracked for about two seconds. This results in a total rotational angle of 2.3°.

R.3 The maximum tracking error is 25 μrad.

R.4 The actuator force should not exceed $\pm$ 4.63 N.[1]

R.5 The actuator voltage should net exceed $\pm$ 24 V.

2.2 Schematic Overview

Figure 1 displays a schematic overview of the system. It is designed such that the desired degree of freedom is satisfied. Here, the mirror which is used to reflect the laser, is colored light grey. This mirror is rigidly connected (yellow mount) to building blocks that are colored dark grey. Two leaf springs are used to keep the system in its equilibrium position, these leaf springs (red) are also connected to the building blocks. The blue block is the motor core, the coil (green) of the motor is actuating up and down in order to achieve the desired rotation. Both the motor and the leaf springs are connected to the fixed world.

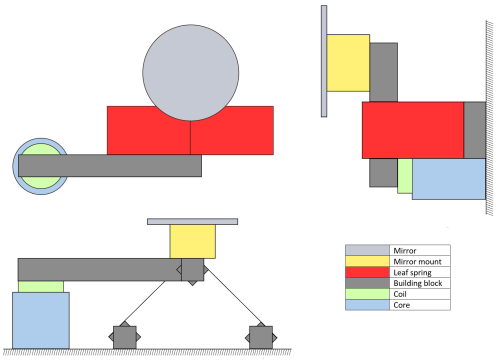

Figure 1: Schematic overview

2.3 Kinematic Structure

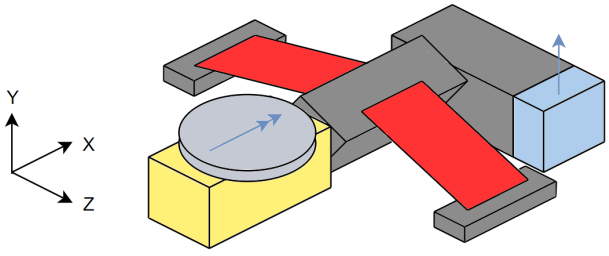

Figure 2: Kinematic overview

Degree of freedom	Constrained by:
Translation X-direction	Arm and leaf springs
Translation Y-direction	Leaf springs
Translation Z-direction	Leaf springs
Rotation X-axis	Free
Rotation Y-axis	Leaf springs
Rotation Z-axis	Leaf springs

Table 1: Overview DOF's

Figure 2 presents the final design. As required, the desired rotational degree of freedom is induced by the VCM actuator. Two leaf springs are used to constrain the system, resulting in one over-constraint. This is due to the

fact that both leaf springs introduce a translational constraint in the x-direction. One of which can eventually be replaced by a notch flexure to resolve the over-constraint. Table 1 shows an overview of the structure's DOF's.

2.4 Deriving the Equation of Motion

Equation 1 displays the equation used to derive the equation of motion (EoM) by means of the Lagrange method.[2] The equation consist of five different partial derivatives where: T is the kinetic energy; D is the energy dissipation; V is the potential energy and Q_i is the generalized force.

$$\frac{d}{dt}(\frac{\partial T}{\partial \dot{q}_i}) - \frac{\partial T}{\partial q_i} + \frac{\partial D}{\partial \dot{q}_i} + \frac{\partial V}{\partial q_i} = Q_i \tag{1}$$

As described in section 2.3, the system only has one degree of freedom which is the rotation about the x-axis described as θ. This means that the independent generalized coordinate q_i of this system is θ.
Below, the equation for the kinetic energy T is given with its contribution in Lagrange's equation.

$$T = \frac{1}{2}J\dot{\theta}^2 \qquad \frac{d}{dt}(\frac{\partial T}{\partial \dot{\theta}}) = J\ddot{\theta}$$

Since the system is assumed to be ideal, there is no dissipation in the system. Hence, D is zero. The potential energy is stored in the leaf springs as a result of the bending of the springs during rotation of the system.
Below, the potential energy V is given with its partial derivative with respect to the independent coördinate θ. c is some rotational spring constant of the leaf springs that is yet to be determined.

$$V = \frac{1}{2}c\theta^2 \qquad \frac{\partial V}{\partial \theta} = c\theta$$

The work function consists of the force F and the displacement $L\sin\theta$. In this, F is the force exerted by the VCM on the arm and $L\sin\theta$ is the vertical displacement of the arm at the point of actuation. The generalized force Q_i is defined as the partial derivative of W with respect to θ.

$$W = FL\sin\theta \qquad Q_i = \frac{\partial W}{\partial \theta} = FL\cos\theta$$

Substituting these equations into Lagrange's equation, the total EoM is obtained as displayed in Equation 2. The linearization of the EoM is obtained using the Taylor series as presented in Equation 3.

$$J\ddot{\theta} + c\theta = FL\cos\theta \tag{2}$$

$$J\ddot{\theta} + c\theta = FL \tag{3}$$

2.5 Nominal Model

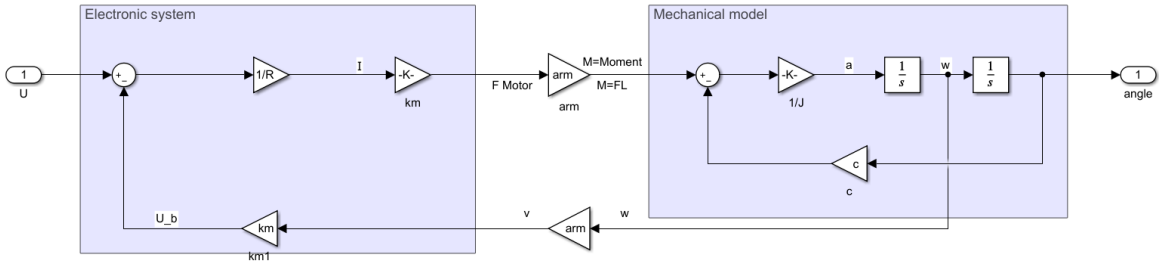

Figure 3: block diagram of the electrical and mechanical domain

A nominal model of the conceptual design was created in Matlab to see whether it meets the requirements.[3] The mechanical part of the nominal model was obtained using the EoM (Eq 3. The electrical part of the nominal model was obtained using provided lecture notes.[4][5] In the nominal model it is assumed that the connections between the actuator, the arm and the mirror are infinitely stiff. In addition, the inductance of the actuator and the mechanical damping are neglected, resulting in a standard second order system. The block diagram of this system is presented in Figure 3. From this diagram the transfer function is deduced, which is shown in Equation 4 where k_m is the motor constant, L is the length of the arm, R is the motor resistance, J is the equivalent inertia and c is the equivalent rotational spring stiffness. The damping term in this equation is a result of the back-EMF.

$$G(s) = \frac{\theta(s)}{U(s)} = \frac{\frac{k_m * L}{R * J}}{s^2 + \frac{k_m^2 * L^2}{R * J}s + \frac{c}{J}} \tag{4}$$

The motor can only handle a maximum continuous force of 4.63 N. In order to stay below this limit, it was decided to take a maximum continuous force of 4 N. In the conceptual design, this translates to a moment on

the mirror equal to the force times the length of the arm. The rotational spring stiffness is chosen such that this moment creates the desired angle. According to Equation 5, the voltage source should deliver 5.56 V in order to achieve this force. An additional 0.014 V is needed to compensate for the back-EMF that is created according to Equation 6 and requirement R.5. These voltages are well within the limits of the actuator. These values result in a current: $I = \frac{U}{R} = 0.54$ A, which is also below the maximum continuous current which lies at 0.63 A.

$$F = \frac{Uk_m}{R} \rightarrow U = \frac{FR}{k_m} \tag{5}$$

$$U_{backEMF} = k_m v = k_m \omega L_{arm} \tag{6}$$

2.6 A Controller Structure

Due to the nature of the satellite application, a very accurate motion is required. As a result, the maximum error during the tracking phase equals 25 μrad. With this maximum error, the crossover frequency of the system can be computed. Firstly, a single PID controller was added to the nominal model. For this combined system of controller and nominal model, a low frequency approximation that has to follow a certain reference is given in Equation 7 with $g_1 = g_2 = g_3 = 0$. A concept design that is modelled using Spacar light, gives a good approximation for the first natural frequency (20 Hz).[6] Reasonable assumptions have been made for the values of α, β and ζ. These values are 0.2, 2 and 0.6 respectively. With these values, the crossover frequency is approximately 400 rad/s during the tracking phase (computed according to Figure 4). A feed forward structure is added, since this increases the performance of the system. This relaxes the requirements on the cross over frequency. Assuming a quality of 0.8 for all types, the crossover frequency of the system is reduced to about 190 rad/s. This can be seen in Figure 5.

$$e_{LF}(t) = \frac{\beta}{\alpha\omega_c^3}((1-g_1)\dddot{r} + (1-g_2)2\zeta\omega_1\ddot{r} + (1-g_3)\omega_1^2\dot{r}) \tag{7}$$

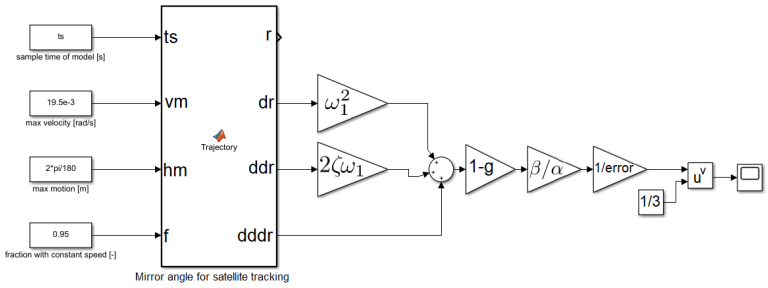

Figure 4: Determination of crossover frequency using Simulink with PID and feedforward

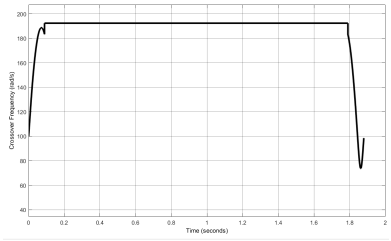

Figure 5: Result of Simulink simulation

The combination of this PID controller with the nominal model of the plant results in an infinite gain margin since the phase does not drop below -180°. The tame PD action of the PID controller delivers a 40° phase margin at the crossover frequency of 190 rad/s. Note that these values are only a proof of concept, because of the assumptions made. Exact numbers will be derived in the detailed design phase when all the plant parameters are known.

3 Design

Before the concept can be implemented, springs and a definitive model have to be designed. Furthermore, a dynamics analysis has to be completed, which is all done in this section.

3.1 Designing the Leaf Springs

Figure 6 shows a schematic overview of the most important parameters in designing the leaf spring dimensions. Using free body diagrams (FBD's), nine equilibrium equations, containing nine unkowns, are found. Resulting in the following relation between F and θ:

$$F = \frac{2 \cdot \theta \cdot E \cdot I}{L_{lf} \cdot (L_1 + L_2)} \tag{8}$$

Since the inertia is given by the following Equation: $I = wt^3/12$, Equation 8 can be rewritten as:

$$L_{lf} = \frac{w \cdot t^3 \theta \cdot E}{3 \cdot F \cdot (L_1 + L_2)} \tag{9}$$

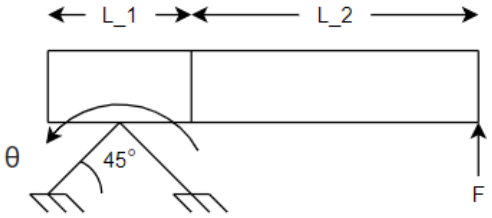

Figure 6: Configuration of the system

Where:

$F = 4$ N $\quad L_1 + L_2 = 81.05$ mm $\quad w = 37.5$ mm $\quad t = 0.6$ mm $\quad \theta = 17.5$ mrad $\quad E = 200$ GPa [7][8]

Substituting these values in Equation 9, results in a spring length of approximately 30 mm. To be able to connect the leaf spring to the design, an additional 12.5 mm is added at both sides. This gave a final spring length of 55 mm.

3.2 CAD Model of the Plant

Taking into account the set design and determined dimensions in sections 2.2, 2.3 and 3.1, a definitive model is created. The CAD model is shown in Figure 7.

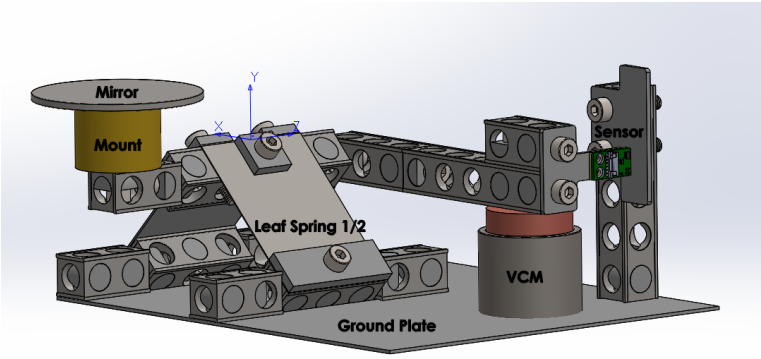

Figure 7: A Solidworks model of the plant

In the model everything is connected using bolts and nuts. What specifically stands out in this model is that the two leaf springs are connected at an angle of 45°. This angle seemed to be the obvious one, with the given hardware set. Since the mirror itself is not located at the axis of rotation, it will experience some translation as well, however this translation will be negligible compared to its rotation. This was verified using Spacar. Besides, the translation of approximately 6 μm is negligible compared to the 30 meter diameter of the laser at the distance of the satellite. It can therefore be concluded that requirement R.1 is met. Furthermore, an additional coordinate system has been added in the model to extract the equivalent inertia of the system at the axis of rotation.

3.3 Dynamic Model

The effects of the parasitic dynamics is determined using Spacar. Here the building blocks are massless bodies because the mass and inertia of the complete mechanical system are included in one node in the Spacar model. All parasitic frequencies beyond the Nyquist frequency of 1 KHz are removed. The results can be seen in Figures 8, 9, 10 and 11.

Mode	Frequency (Hz)
1	10.74
2	325.4
3	332.4
4	514.7
5	517.1
6	570.7
7	648.8

Table 2: Overview Modes

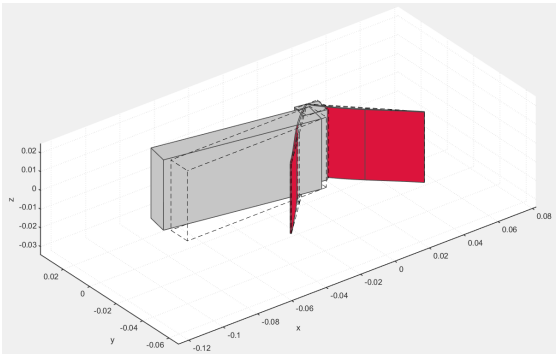

Figure 8: First mode: Naturalfrequency

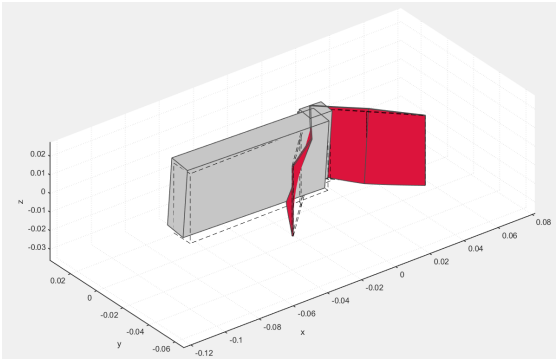

Figure 9: Second mode: Parasitic frequency

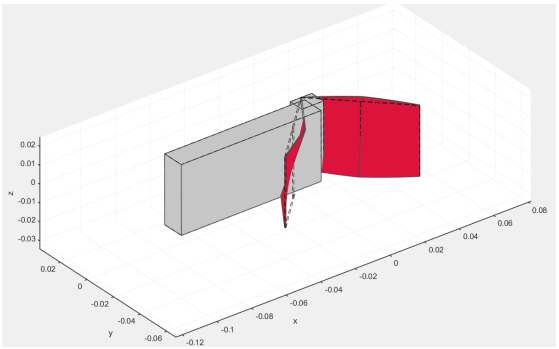

Figure 10: fourth mode: Internal mode

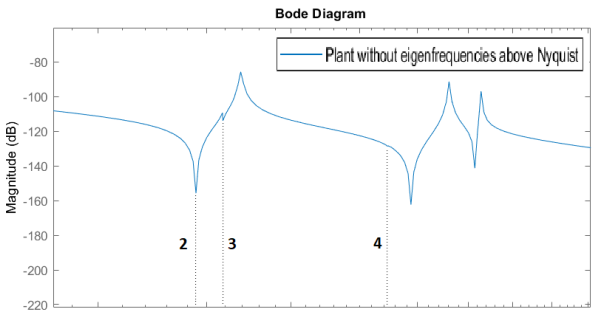

Figure 11: Internal modes in the phase plot

In Table 2 all modes with corresponding frequencies below the nyquist frequency are displayed. The first mode is the desired mode since this causes the desired rotation of the mechanical structure. Some insight can be obtained by taking a closer look at mode 2 and 4, shown in Figures 9 and 10 respectively. Mode 2 is a parasitic mode, since it influences the sensor reading. However, the third and fourth mode are internal modes and are invisible for the sensor. This can be understood by looking at the bode plot in Figure 11. Since the sensor can not see the third and fourth mode, there will be no resonance peaks in the bode plot at the frequencies of the third and fourth mode.

3.4 Discretization

To be able to control the mechatronic system digitally, it has to be discretized. Discretization is a positive step towards a controllable system, since a digital controller is easier to tweek than an analog controller. The downside is that low and high-frequent data is lost. Taking this into account, the sampling frequency is set to $40\omega_c$. A Zero Order Hold (ZOH) discretization is used on the data of the electro-mechanical model obtained from Spacar, while Tustin's method is used on the PID controller. Tustin's method provides the best approximation for the phase. This is desired in the PID controller, since a phase lead was introduced in the PID. The resulting bode plot can be seen in Figure 13.

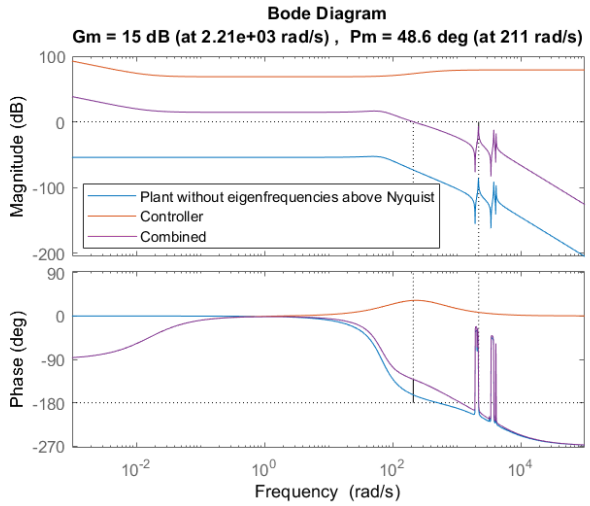

Figure 12: Bode plot analog

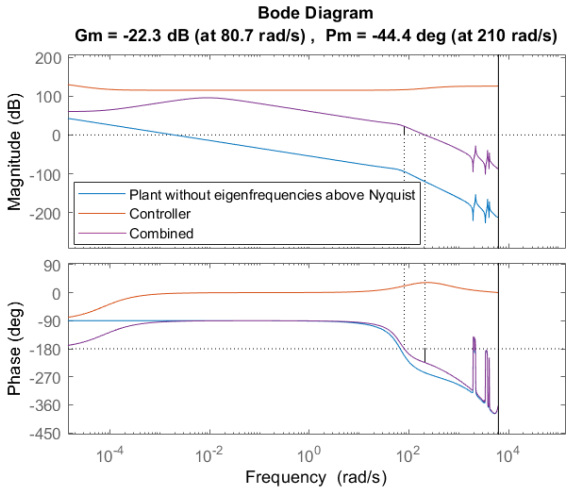

Figure 13: Bode plot discretized

3.5 Effect Analysis and Trade-Offs

Effect Analysis From the bode plot it follows that the system is stable, mostly due to the fact that the controller ensures a 48° Phase Margin and only one crossing of the zero dB line. The parasitic dynamics give a couple of (anti)resonances, because the anti resonance precedes the resonance which indicates collocated control (which is indeed the case) a positive jump of 180° is perceived. This might cause some trouble, luckily the gain stays below zero dB and unstable behaviour is avoided. Furthermore the discretization described above only has the slightest effect on the phase margin. The gain margin is influenced a bit more, the higher order dynamics have been pushed down, so the smallest gain margin is now at 81 rad/s and -22.3 dB (Figure 13). As a double check, the Nyquist plots show no encirclement of -1, thus the system is stable.
The effect of the sampling frequency is rather big on the stability margins. The bode plots above are sampled at a frequency 40 times bigger than the crossover frequency at 1.3 kHz. If we would reduce the sample time we would lose a lot of the higher order dynamics. The model has been sampled at the maximum frequency the hardware would allow to check whether the parasitic behaviour causes instability. This was not the case so the sampling frequency was kept at 40 times the crossover frequency to reduce the computational time.

An additional delay has been added to the system to account for the unavoidable computational time. The delay comes with a slope of -20 [dB/decade] at a crossover frequency of 1 rad/s. It also adds a phase shift of $-90°$ for all frequencies, as can be seen in Figure 14. To compensate for the gain the controller parameters should be retuned to end up with the required crossover frequency. After the retuning, the steeper slope pushes the parasitic dynamics even further below 0 dB and the gain at 80 rad/s further above 0 dB which causes the gain margins to increase. The phase margin shifts from a positive 45° to a negative 45°, which is still stable.

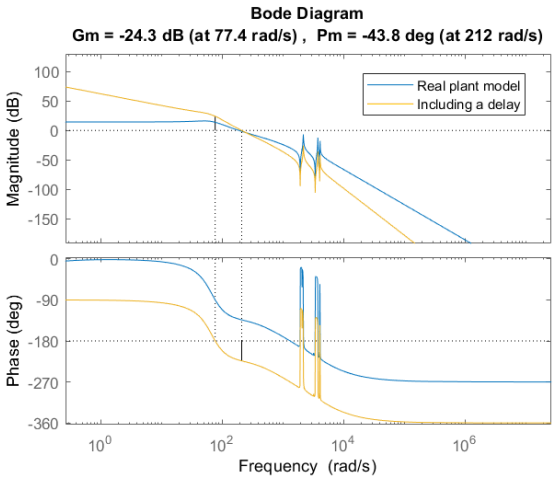

Figure 14: Effect of a single delay

Trade-Offs In section 3.1 the leaf spring dimensions were determined using a maximum motor force of 4 N. During modeling, Spacar found a first eigenfrequency of 20 Hz, which is not favorable considering a crossover frequency of 30 Hz. The first eigenfrequency is equally influenced by the spring stiffness and the inertia. The spring stiffness is proportional to the thickness to the power three (Eq 8). Lowering the spring stiffness also decreases the frequencies of parasitic modes which brings them closer to the crossover frequency. That could bring the resonance peaks above the zero dB line, possibly resulting in instability. The sweet spot was found at a thickness of 3 mm, resulting in a first eigenfrequency of 10 Hz. An additional advantage is that the required force is reduced significant, reducing wear and tear of the actuator.
A second trade off has been made with the controller settings. A higher alpha would lead to more phase margin

but at the same time it increases the crossover frequency according to Equation 7. In principle, there is no limit on the crossover frequency, but it should not be too close to the parasitic frequencies to prevent the resonance to cross the zero dB line. Besides the sampling frequency is related to the crossover frequency and limited by the hardware. Alpha has been kept at 0.2 resulting in enough phase margin ($\sim 45°$) and a desirable crossover frequency.

4 Implementation

All findings in the previous chapter have to be implemented in the model. In this chapter the result of that implementation is simulated.

4.1 Controller

As explained in section 2.6, a PID-controller is used to control the electro-mechanical system. The problem with a standard PID-controller is that high frequent noise will increase the output of the D-action significantly, which is unwanted. Therefore, a low pass filter is implemented in the discretized PID controller as shown in Figure 15. An integrator anti wind-up is implemented such that the output of the controller does not exceeds certain values. The limits of this integrator anti wind-up are set based on requirement R.4. The controller actions are tuned in such a way that the error of the system is within the boundaries set in the requirements.

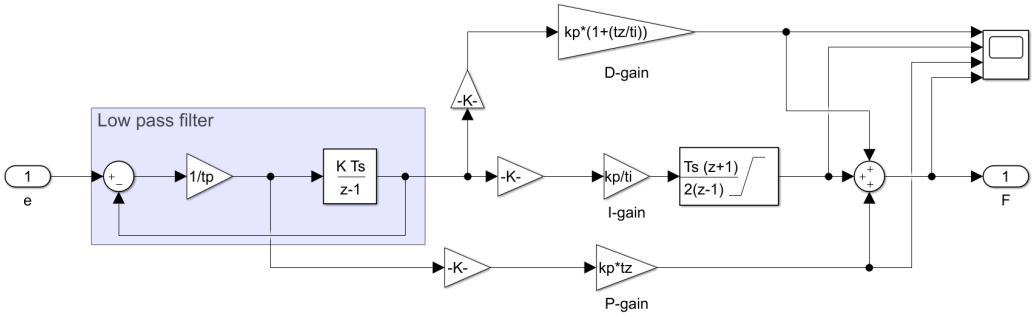

Figure 15: An overview of the implemented PID-controller.

4.2 Model

The block diagram of the simulation of the closed loop system can be seen in Figure 16. The system contains the discretized PID-controller discussed in section 4.1. The reference signal is the output of the "Trajectory" block seen on the left.

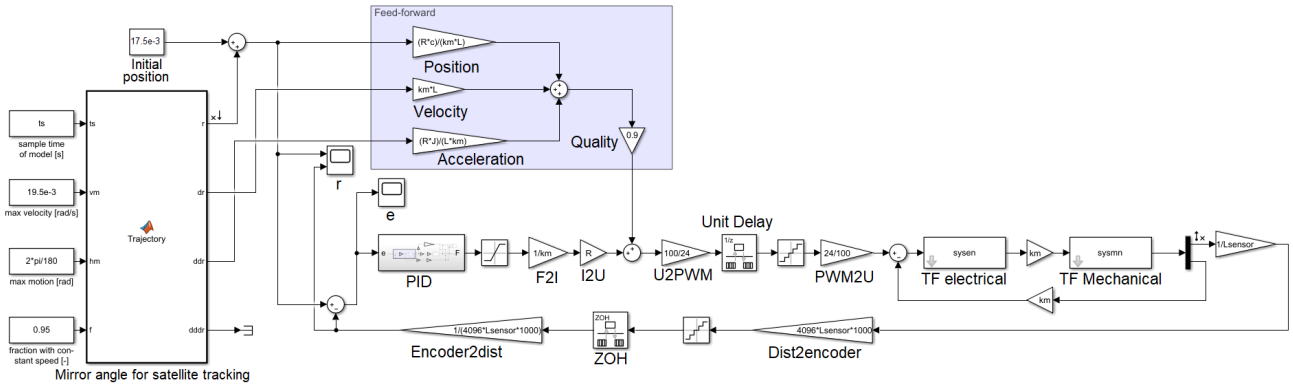

Figure 16: An overview of the Discrete system

After the PID-controller, the signal is converted into a PWM signal. Consequently, a unit delay is added and the signal is discretized. This is done by the rate-transition and quantizer blocks.
Since the sensor measures position in encoder counts, the feedback signal needs to be converted back to radians. As a result, the signal is multiplied by the gain derived in Equation 10. Note that due to the small change in

angle, the sine term converts to 1, since it is linearized using the Taylor series.

$$\theta = \sin \frac{1}{L \cdot 4096 \cdot 10^3} \approx (L \cdot 4096 \cdot 10^3)^{-1} \tag{10}$$

Here, θ is the position of the system in radians, this position is fed back to the system in order to calculate the error. The distance between the sensor and the point of rotation is denoted by L. The sensor measures 4096 counts for every millimeter, therefore the denominator is multiplied by a factor $4096 \cdot 10^3$.[9]
To anticipate for future behaviour, a feed-forward is added to reduce the error and improve the stability of the system. In the feed-forward system: Position is used to compensate for the velocity; velocity is used to compensate for the acceleration and acceleration is used to compensate for the jerk. They are defined below.

$$\text{Position: } \frac{R \cdot c}{km \cdot arm} \;\Big|\; \text{Velocity: } km \cdot arm \;\Big|\; \text{Acceleration: } \frac{R \cdot J_{tot}}{km \cdot arm}$$

The feed-forward is designed such that it is the inverse of the transfer function. Since we cannot predict the inverse of the transfer function perfectly in real life, the feedforward is multiplied by a quality factor 0.9.

5 Verification

The established design should be verified to ensure that the mechanism behaves as expected and if it meets the functional requirements.

5.1 Verification of the Design

In Figure 17 the results of the linearity check is shown which is done with the use of Simulink. This is achieved by changing the input voltage between the minimum and maximum. The result is a completely linear system, as expected since the system is simulated and not tested in real life, where energy dissipation could disturb the linear behaviour.
By multiplying the voltage with the motor constant and dividing it by the resistance of the motor, the actuator force is given. The actuator force divided by the angle in radians gives the stiffness of the system, which is equal to 0.72 N/rad. In the model a stiffness of 1.16 N/rad was used, this difference is caused due to the fact the model has no resistance force.
Figure 18 shows the frequency response from a chirp input signal. The low frequent magnitude of the modelled transfer function is -54.2 dB, which results in a static gain of $2.0 \cdot 10^{-3}$. The low frequent magnitude of the frequency response is -31 dB, which results in a static gain of $2.8 \cdot 10^{-2}$.

$$G(s) = K \cdot \frac{\omega_n^2}{s^2 + 2\zeta\omega_n \cdot s + \omega_n^2} \tag{11}$$

A new transfer function is made that would better fit the frequency response in the form of Equation 11, this is the green line in Figure 18. For the transfer function the following values were used: ω_n is 70 rad/s, ζ is 0.5 and static gain of $2.8 \cdot 10^{-2}$. With this fitting transfer function the inertia and damping are calculated. The calculated inertia is $1.5 \cdot 10^{-4}$ Kgm^2, where it was modelled as $5.3 \cdot 10^{-4}$ Kgm^2. With this new inertia, the damping coefficient is calculated, namely 0.01 Ns/rad, compared to the modelled damping coefficient of 0.03. Both inertia and damping are a factor of three smaller than modelled.

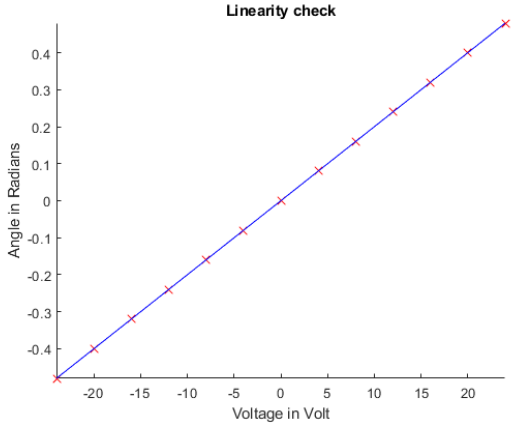

Figure 17: Linearity check

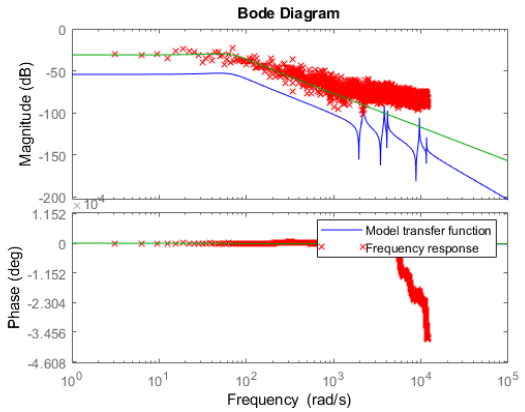

Figure 18: Frequency response

5.2 (Re)design of the Controller

After the implementation and verification of the design using Simulink models, it has become clear that the designed controller in section 2.6 was not sufficient. The controller gains have been changed in section 3.5 to account for the additional delay. Furthermore, the proportional, differentiating and integrating gains have been tuned in section 4.1 to meet the error requirements. This fine-tuning led to a crossover frequency higher than calculated in section 2.6. The bode diagram subtracted from Figure 16 with the reference as an input and the position as a output, indicates a crossover frequency of 300 rad/s. This is still well below four times the first parasitic frequency of 2042 rad/s. The stability margins have not been influenced a lot during the verification phase and are still in line with Figure 13 at GM = 15 dB and PM = 42 °.

5.3 Verification of the performance

In order to verify the performance, the system (and model) have to meet the requirements. In Figure 19 the trajectory to be followed can be seen in red (requirement R.2). Also, in the same figure the simulated output of the system is plotted in blue. They cannot be distinguished, therefore a zoomed plot is shown in Figure 20. Here, the red line is again the set trajectory and the blue line the output of the system. From these two figures it can be concluded that the systems output speed of 19.5 rad/s is the same as the preset trajectory speed, therefore requirement R.2 is met.

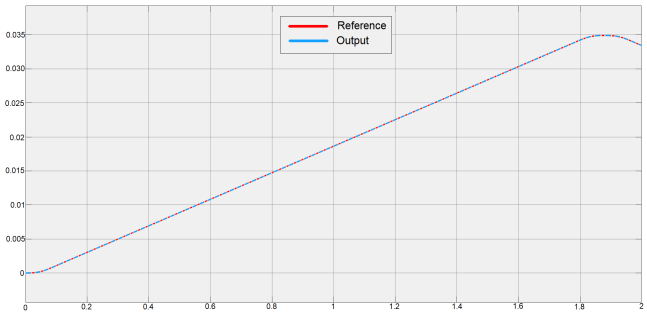

Figure 19: A graph of the trajectory of the system

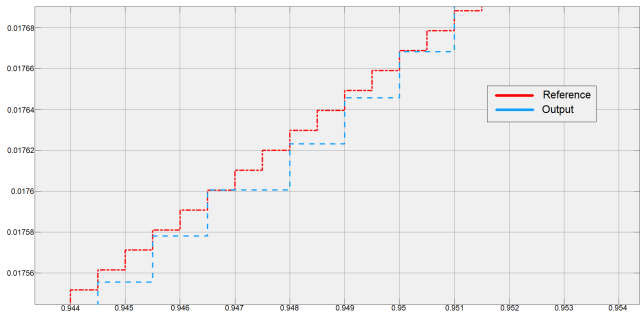

Figure 20: Zoom of the trajectory to show discretization

A deeper insight in the performance can be obtained by looking at what the value of the error is. In order to meet requirement R.3, the steady state error may not exceed 25 μrad. Figure 21 displays the error. According to the peak finder function, the maximum error during the entire motion is 21.48 μrad at t= 0.977 s and thus it is verified that requirement R.3 is met. Requirements R.4 and R.5 stated that the maximum actuator force cannot exceed ±4.63 N and the maximum voltage cannot exceed ±24 V respectively. In Figure 22, the system results are shown. The limits on the actuator voltage and force are respected and both requirements R.4 and R.5 are met. The motor only has to deliver little force and receive little voltage additionally, since it starts in its initial position already. That means that most of the energy is already available as potential energy in the leaf springs.

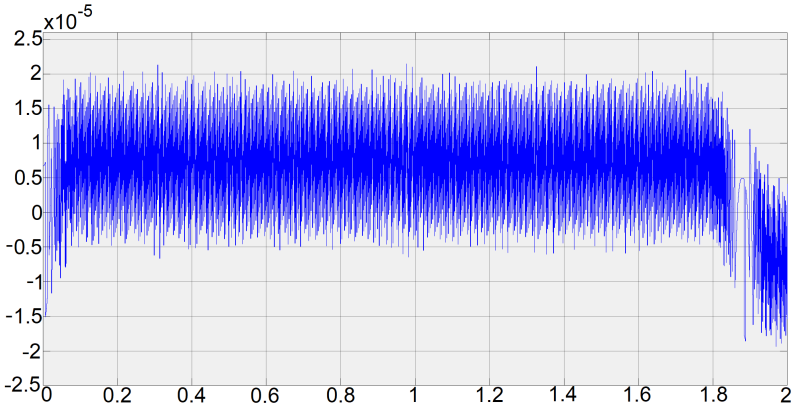

Figure 21: Graph of the error of the system

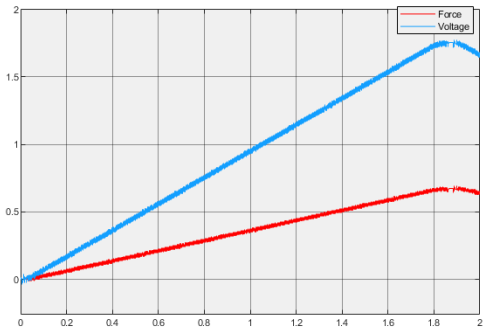

Figure 22: A graph to show that the motor Force and Voltage are within the limits

5.4 Comparison of Simulation and Design

In section 2.5 and 2.6, the nominal model was presented. The performed calculations will be compared to the final outcome. Previously, it was determined that the required voltage was 5.6 V, however according to Figure 22 the actual maximum voltage is equal to 1.8 V. This can be traced back to the modification of the spring thickness during the redesign of the electro-mechanical system and the controller. The inertia was also found to

be smaller (section 5.1) than in the initial model, which also explains a lower required voltage. The voltage and force are related according to Eq 5, in Figure 22 this relation is not satisfied. This is caused by the addition of the quantizer.

5.5 Evalution of the design

In order to evaluate the design properly, it is checked whether the design satisfies the functional requirements that where set at the start of this project. Almost all the requirements are met. Firstly, the tracking error at the start of the constant velocity phase is within limits of 25 μrad. Secondly, the rotational speed of the mirror is 19.5 $mrad/s$. Lastly, the actuator force and actuator voltage do not exceed the set values of ± 4.63 N and ± 24 V respectively. However, the design does not comply with the requirement that limits it to having one degree of freedom. This is due to the shortening of the leaf springs, which occurs during rotational displacement, resulting in translations in the x- and y-direction. Moreover, the mirror does not lie perfectly on the point of rotation. As a result, additional translations are introduced. Since these translations are very small compared to the rotational displacement and all the other requirements are met, the overall performance of the system is acceptable.

6 References

[1] TDS Precision Products. *(Standard Series) AVM.*

[2] Ir. B.M. de Gooijer Dr.Ir J.P. Schilder. Mechanical vibrations (065). 04/2019.

[3] The Mathworks, Inc. *MATLAB R2018b*, 2018.

[4] R. G. K. M. Aarts and J. van Dijk. Design and control of mechatronic systems part 1 (730). 08/2018.

[5] R. G. K. M. Aarts and J. van Dijk. Design and control of mechatronic systems part 2 (089). 04 2019.

[6] *Spacar Light*, 2017. `http://www.spacar.nl/wiki/doku.php?id=overview`.

[7] *Data for spring design (1).* `https://canvas.utwente.nl/courses/5323/files/1493717/download?wrap=1`.

[8] *Data for spring design (2).* `https://canvas.utwente.nl/courses/5323/files/1493716/download?wrap=1`.

[9] RLS. *RLB miniature PCB level incremental magnetic encoder sensor system*, 9 2017. Issue 4.